Article

Sustainable conversion of alkaline nitrate to ammonia at activities greater than 2 A cm^{-2}

Check for updates

Wanru Liao [1,9], Jun Wang [1,9], Ganghai Ni[1], Kang Liu[1], Changxu Liu [2], Shanyong Chen[3], Qiyou Wang[1], Yingkang Chen[1], Tao Luo[1], Xiqing Wang[1], Yanqiu Wang[3], Wenzhang Li[3], Ting-Shan Chan [4], Chao Ma [5], Hongmei Li[1], Ying Liang [6], Weizhen Liu[7], Junwei Fu[1] ✉, Beidou Xi [8] ✉ & Min Liu [1] ✉

Nitrate (NO_3^-) pollution poses significant threats to water quality and global nitrogen cycles. Alkaline electrocatalytic NO_3^- reduction reaction (NO_3RR) emerges as an attractive route for enabling NO_3^- removal and sustainable ammonia (NH_3) synthesis. However, it suffers from insufficient proton (H^+) supply in high pH conditions, restricting NO_3^--to-NH_3 activity. Herein, we propose a halogen-mediated H^+ feeding strategy to enhance the alkaline NO_3RR performance. Our platform achieves near-100% NH_3 Faradaic efficiency (pH = 14) with a current density of 2 A cm^{-2} and enables an over 99% NO_3^--to-NH_3 conversion efficiency. We also convert NO_3^- to high-purity NH_4Cl with near-unity efficiency, suggesting a practical approach to valorizing pollutants into valuable ammonia products. Theoretical simulations and in situ experiments reveal that Cl-coordination endows a shifted d-band center of Pd atoms to construct local H^+-abundant environments, through arousing dangling O-H water dissociation and fast *H desorption, for *NO intermediate hydrogenation and finally effective NO_3^--to-NH_3 conversion.

Nitrate (NO_3^-) is one of the most widespread water contaminants, sourced from agricultural runoff and industrial sewage discharges, that disharmonizes the global nitrogen cycle[1–4]. The presence of NO_3^- pollution in water bodies is a matter of significant environmental concern due to its detrimental impacts on both aquatic ecosystems and human health. Excessive NO_3^- concentrations can lead to eutrophication[5], the depletion of dissolved oxygen, and the production of harmful algal blooms. Ingesting water with high NO_3^- levels can also have adverse health effects, inducing problems such as cancer[6] and the commonly known blue-baby disease[7].

To address the pressing challenges posed by NO_3^- pollution, tremendous efforts have been made to develop cost-effective methods for NO_3^- removal, ranging from reverse osmosis, ion exchange, electrocatalysis to electrodialysis and biological denitrification[8,9]. Among them, electrocatalysis is the most promising solution[10–12], performed under mild conditions with high selectivity, versatility and environmental sustainability[1,13–16]. Within this scope, electrocatalytic NO_3^- reduction reaction (NO_3RR), which converts NO_3^- to ammonia (NH_3) with renewable electricity inputs, offers an operational avenue for restoring the disturbed nitrogen cycle and facilitating the

[1]Hunan Joint International Research Center for Carbon Dioxide Resource Utilization, State Key Laboratory of Powder Metallurgy, School of Physics, Central South University, Changsha 410083, PR China. [2]Centre for Metamaterial Research & Innovation, Department of Engineering, University of Exeter, Exeter EX4 4QF, UK. [3]School of Chemistry and Chemical Engineering, Central South University, Changsha 410083, PR China. [4]National Synchrotron Radiation Research Center, Hsinchu 300092, Taiwan. [5]College of Materials Science and Engineering, Hunan University, Changsha 410082, PR China. [6]College of Food Science and Engineering, Central South University of Forestry and Technology, Changsha 410004, PR China. [7]School of Environment and Energy, Guangdong Provincial Key Laboratory of Solid Wastes Pollution Control and Recycling, South China University of Technology, Guangzhou 510006, PR China. [8]State Key Laboratory of Environmental Criteria and Risk Assessment, Chinese Research Academy of Environmental Sciences, 100012 Beijing, PR China. [9]These authors contributed equally: Wanru Liao, Jun Wang. ✉e-mail: fujunwei@csu.edu.cn; xibd@craes.org.cn; minliu@csu.edu.cn

denitrification of wastewater, as well as a sustainable alternative to the energy-intensive Haber-Bosch techniques that consume 2% of the world's energy and release 1.4% of global carbon dioxide emissions[17–21]. Tackling NO_3^- in high pH systems is of particular interest owing to its practical applications toward industrial and agricultural wastewater[22] and less formation of toxic nitrogen oxide byproducts[23–25].

In the past five years, significant advancements have been made in the field of alkaline NO_3RR to NH_3 synthesis, utilizing a repertoire of catalysis, including Cu encapsulated in a porous carbon framework[26], Fe-based single-atom catalysts (SACs)[27], CuPd nanocubes[24], strained Ru nanoclusters[28], reduced-graphene-oxide-supported RuCu alloy[29], and $Cu_{50}Ni_{50}$ alloy[30]. In spite of continuous improvements in Faradaic efficiency (FE), a close-to-100% value was only reported under moderate NH_3 yield rates (<10 mg h^{-1} cm^{-2}) and limited current density (<300 mA cm^{-2})[28–31]. Further increasing the current density and production rate have been accompanied by a degradation of the FE[18,23]. Given the pressing challenge of wastewater containing NO_3^- resulting from urbanization and population growth, alkaline electrocatalytic system for NO_3^- reduction with both high NH_3 FE (>95%) and fast reaction rates (>1 A cm^{-2}) is of pivotal importance for a sustainable future, but remains elusive.

In this study, we design and realize a halogen-mediated alkaline electrocatalytic platform to overcome the limitation and achieve high-speed conversion of NO_3^- to NH_3 while maintaining an ideal FE. Modifying Pd species on Cu_2O platform with excellent NO_3^- adsorption and conversion ability[32,33] could favor H_2O dissociation under high pH conditions[34–36]. But the intense interaction between the *d* orbitals of Pd and *s* orbitals of *H (* denotes the adsorbed state) brings strong Pd-H binding[37], which affects the desorption of *H. Halogen elements with high first-electron-affinity[38] can tailor the $3d$ orbital electron structure of Pd atom to regulate *H release, thereby breaking the bottleneck of FE due to the scarce proton (H$^+$) feeding in high pH conditions. Here we develop Cl-coordinated Pd SACs-dispersed Cu_2O matrix (Pd-Cl/Cu_2O) nanocrystal to carry out alkaline NO_3RR. As a result, we simultaneously achieve a NH_3 FE of ~100% with a current density of ~2 A cm^{-2} for 1 h and NH_3 yield rate of ~330 mg h^{-1} cm^{-2} at 1 M NO_3^- concentration (pH = 14), outperforming previous results with large current densities[23,39,40]. Impressively, our platform can reduce the NO_3^- concentration from an industrial wastewater level of 56 mM to a drinkable water level (<0.8 mM), with an over 99.1% NO_3^--to-NH_3 conversion efficiency. Further, we demonstrate a successful conversion of NO_3^- into practical ammonia products with near-unity efficiency via coupling the NO_3RR with an air stripping process. The combined results of in situ Raman spectroscopy, in situ attenuated total reflection infrared spectroscopy (ATR-IR), kinetic isotope effect (KIE) experiments, and theoretical simulations reveal that Cl-coordination induces a shifted *d*-band center

of Pd atoms to construct local H$^+$-abundant environments, through triggering the dissociation of dangling O-H water and fast *H desorption for *NO intermediate hydrogenation and finally efficient NO_3^--to-NH_3 conversion (Fig. 1). This tactic can be extended to other halogen element Pd-(F, Br, I)/Cu_2O for alkaline NO_3RR to NH_3, demonstrating the wider applicability of the halogen-mediate strategy.

Results
Theoretical prediction

To test the halogen mediating effect, density functional theory (DFT) calculations were conducted on the models of Cu_2O, Pd-dispersed Cu_2O (Pd/Cu_2O) and Pd-Cl/Cu_2O with different Cl numbers (Supplementary Figs. 1, 2). Cu_2O showed a high Gibbs free energy change for H_2O dissociation (ΔG_{H_2O} of 1.19 eV, Fig. 2a), while the corresponding value on Pd/Cu_2O (0.70 eV) decreased, indicating the accelerated H_2O dissociation under the assistance of Pd SACs. The introduction of Cl coordination endowed Pd-Cl/Cu_2O model (optimized model of Pd atoms coordinated with two Cl, Supplementary Fig. 3) with a further decrease of ΔG_{H_2O} (0.68 eV) and more favorable to generate H$^+$ (ΔG_{H^+} of −1.34 eV).

To investigate the influence of Cl coordination on the H$^+$ formation, differential charge distribution and the local density of states (LDOS) were calculated. From the charge density difference (Fig. 2b), the two Cl atoms on Pd-Cl/Cu_2O both obtained 0.47 *e*, which was supplied by the coordinated Pd atom (0.13 *e*) in addition to the contribution from the Cu_2O substrate. The Cl ligand with strong first-electron-affinity seized the electrons of Pd[38] and induced a downward shifted $3d_{xy}$ and $3d_{z^2}$-band center of Pd atom in Pd-Cl/Cu_2O compared to that of Pd/Cu_2O, as well as a upward shifted $3d_{xz}$-band center of Pd (Fig. 2c). Thus, under the regulation of Cl ligand, the shifted *d*-band center of Pd enabled *H on the catalyst to obtain more electrons (0.13 *e*) and make *H more unstable to promote the H$^+$ release (Fig. 2b).

Next, after considering the effects of potential and pH on NO_3RR pathway with multiple possible branches (Supplementary Figs. 4−6), the optimal pathway on Cu_2O, Pd/Cu_2O and Pd-Cl/Cu_2O models at the potential of −0.6 V vs. RHE for pH = 14 was proposed and the corresponding ΔG of each intermediate was calculated (Fig. 2d and Supplementary Figs. 7, 8). In such a sequential electron−proton transfer process (Supplementary Fig. 9)[41,42], the hydrogenation of *NO_2 into *NO_2H (*NO_2 + H_2O + e^- → *NO_2H + OH^-) was the potential-determining step (PDS), which involved a ΔG of −0.57 eV over pure Cu_2O. Pd/Cu_2O also presented a relatively lower ΔG of PDS (−0.65 eV). Pd-Cl/Cu_2O showed the lowest ΔG of PDS (−0.76 eV) and correspondingly advanced the progress of NO_3RR. Thus, Pd-Cl/Cu_2O was anticipated as a promising candidate for alkaline NO_3RR towards NH_3 synthesis.
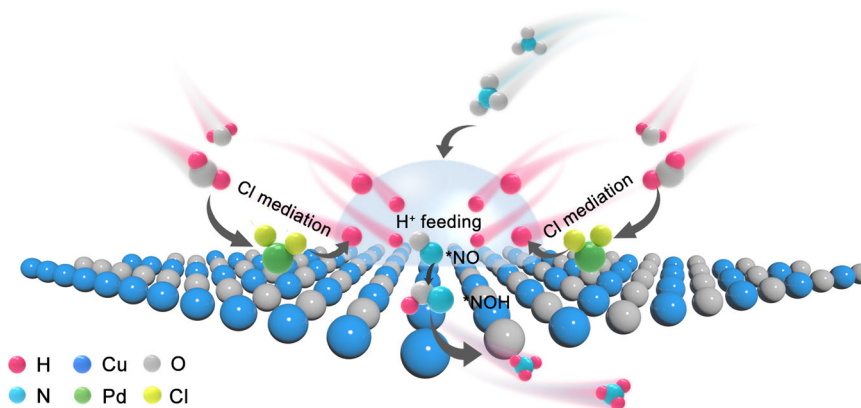

Fig. 1 | Cl mediated H$^+$ feeding. Schematic diagram of Cl mediated H$^+$ feeding to boost *NO intermediate hydrogenation and finally achieve efficient NO_3^--to-NH_3 conversion in alkaline NO_3RR over Pd-Cl/Cu_2O.
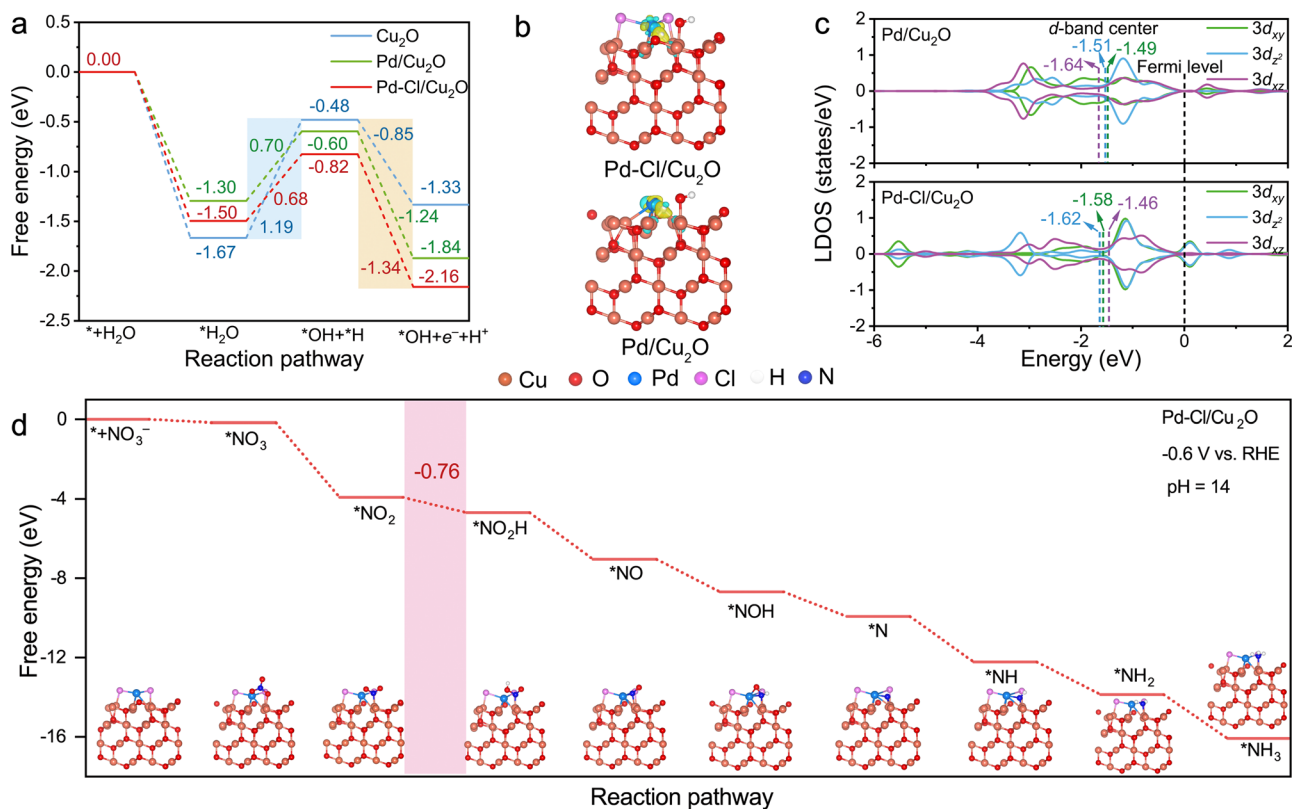
Fig. 2 | Theoretical prediction. a Gibbs free energy change of H$^+$ supply over catalysts. **b** The charge density difference between *H intermediate and catalysts. The isosurface level was 0.005 e·bohr^{-3}. The yellow and cyan colors represented positive and negative charge regions, respectively. 0.13 e was the electrons transferred from Pd-Cl/Cu$_2$O to *H, and 0.09 e was the electrons transferred from Pd/Cu$_2$O to *H. **c** The local density of states of Pd 3d orbital for the Pd/Cu$_2$O and Pd-Cl/Cu$_2$O catalysts. **d** Gibbs free energy diagram of various intermediates generated during NO$_3$RR over Pd-Cl/Cu$_2$O at the potential of −0.6 V vs. RHE for pH = 14.

Synthesis and structural characterizations of catalysts

Inspired by the theoretical results, we synthesized Cu$_2$O, Pd/Cu$_2$O and Pd-Cl/Cu$_2$O catalysts (see details in Methods). Scanning electron microscopy (SEM), transmission electron microscopy (TEM) and high-resolution TEM (HRTEM) showed Cu$_2$O had a lotus-like morphology on Cu foam with the orientation of (111) crystal planes (Supplementary Figs. 10–15). Pd-Cl/Cu$_2$O and Pd/Cu$_2$O maintained similar morphology to the initial Cu$_2$O (Fig. 3a and Supplementary Figs. 16, 17). X-ray diffraction (XRD) patterns only presented the peaks of Cu$_2$O and no Pd signals in these catalysts (Supplementary Fig. 18). The corresponding energy-dispersive X-ray (EDX) elemental mapping indicated the uniform distribution of Pd species on the Cu$_2$O matrix (Fig. 3b and Supplementary Fig. 19). The Pd appearing as the bright and isolated atoms was observed by aberration-corrected high-angle annular dark-field scanning transmission electron microscopy (AC-HAADF-STEM) images (Fig. 3c and Supplementary Fig. 20), confirming the successful preparation of Pd SACs in Pd-Cl/Cu$_2$O and Pd/Cu$_2$O.

To explore the electronic structure of Pd SACs, high-resolution X-ray photoelectron spectroscopy (XPS) measurements were performed. The Cu 2p XPS and Cu LMM Auger spectra (Supplementary Fig. 21a, b) identified that Cu^{1+} existed in all samples[43,44]. Pd 3d spectra displayed the binding energies of Pd$^{\delta+}$ (0 < δ < 2) species in Pd-Cl/Cu$_2$O positively shifted compared with Pd/Cu$_2$O (Supplementary Fig. 21c)[45], indicating the electron overflow on Pd in Pd-Cl/Cu$_2$O. In the Cl 2p spectra, obvious Cl signals of Pd-Cl/Cu$_2$O proved the presence of Cl, while not observed in Pd/Cu$_2$O (Supplementary Fig. 21d). The binding energies of Cl peaks negatively shifted 0.3 eV compared to those of commercial PdCl$_2$ (Supplementary Fig. 22), revealing the electron-enriched Cl species in Pd-Cl/Cu$_2$O[46,47]. Combined with the results of Cl 2p and Pd 3d spectra, it can be concluded that the electron transferred

from Pd to Cl in Pd-Cl/Cu$_2$O under the Cl mediation, consistent with DFT calculation analysis.

To ascertain the coordination structure of catalysts, X-ray absorption fine structure (XAFS) was investigated. The Pd K-edge X-ray absorption near edge structure (XANES) spectra exhibited the pre-edge absorption energy of Pd-Cl/Cu$_2$O and Pd/Cu$_2$O located between those of Pd foil and PdCl$_2$ references (Fig. 3d and Supplementary Fig. 23a), implying the valence state of Pd within 0 to 2. The Fourier transformed (FT) extended X-ray absorption fine structure (EXAFS) suggested the absence of Pd-Pd scattering (2.5 Å) in both catalysts, verifying the single-atom dispersion of Pd. The main peak at 2.1 Å for the Pd-Cl/Cu$_2$O can be deconvoluted into 1.8 Å and 2.2 Å scattering (Fig. 3e), ascribing to Pd-Cl and Pd-Cu coordination structures, respectively. The quantitative least-squares best-fitting of EXAFS spectra (Fig. 3f and Supplementary Table 1) confirmed that Pd center was coordinated with ~2 Cl atoms and ~3 Cu atoms (Fig. 3f, inset). By comparison, Pd atom in Pd/Cu$_2$O only coordinated with ~3 Cu atoms (Supplementary Figs. 23b, c and Table 2). The high-resolution wavelet transform (WT) EXAFS plots in K spaces further demonstrate the existence of Pd-Cl coordination in Pd-Cl/Cu$_2$O, but absence in Pd/Cu$_2$O (Supplementary Fig. 24). These results suggested the successful synthesis of the Pd-Cl/Cu$_2$O and Pd/Cu$_2$O catalysts, as proposed in DFT simulation.

NO$_3^-$ intermediates hydrogenation.

To probe H$^+$ feeding on halogen-mediated samples, in situ Raman spectra were carried out (Supplementary Fig. 25). For the Pd-Cl/Cu$_2$O (Fig. 4a), the stretching vibration peak of H$_2$O at 1615 cm^{-1} appeared at 0.1 V vs. RHE and then shifted to 1605 cm^{-1} as the potential decreased to −0.8 V vs. RHE, indicating a weaker H-bond of interfacial H$_2$O to enable H$_2$O dissociation[48–50]. Notably, the emerging H$_3$O$^+$ peak (1770 cm^{-1}) proved that the *H
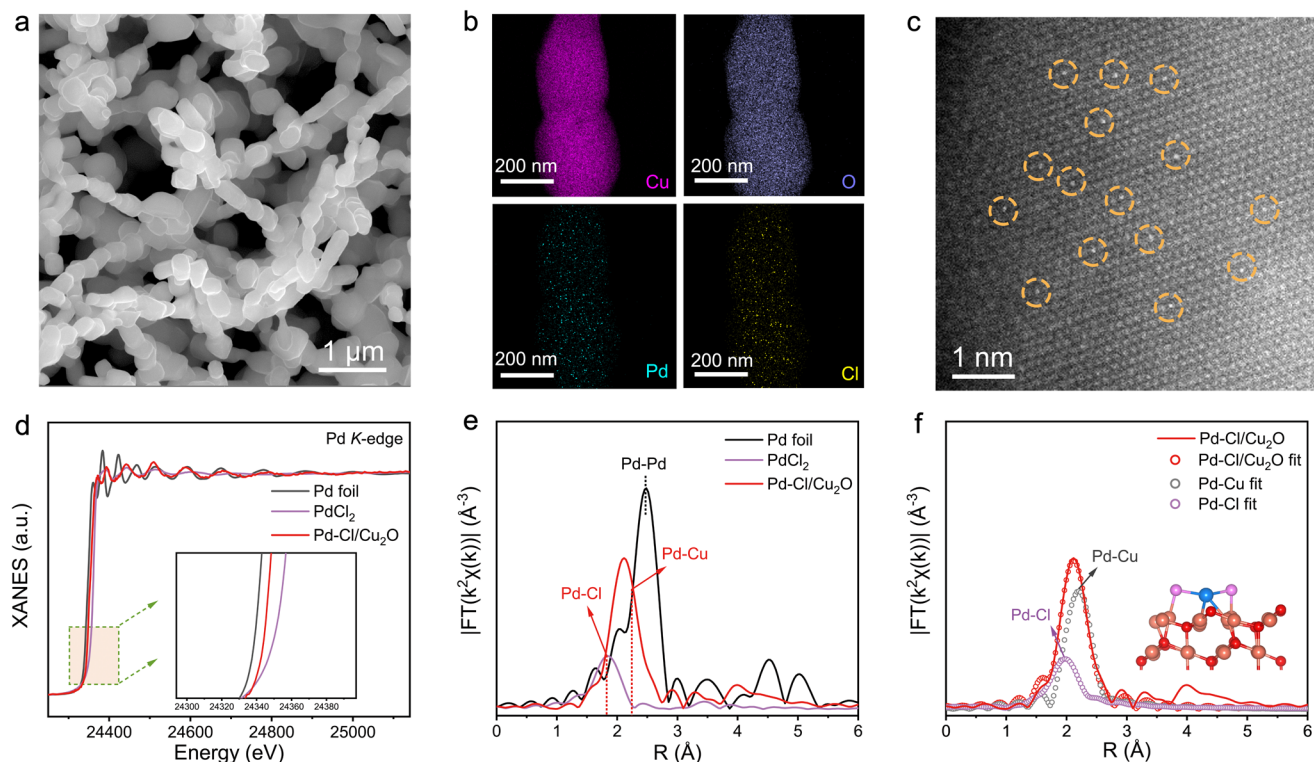
Fig. 3 | Synthesis and structural characterizations of Pd-Cl/Cu₂O. SEM (**a**), EDX mapping (**b**), and AC-HAADF-STEM images (**c**) of Pd-Cl/Cu₂O. Pd K-edge XANES spectra (**d**), and FT k^2-weighted EXAFS spectra (**e**) of Pd-Cl/Cu₂O and reference samples. **f** The fitting EXAFS spectra of Pd-Cl/Cu₂O. Inset: fitting model.

generated by H_2O dissociation was immediately desorbed from Pd-Cl/Cu_2O surface, to construct local H^+-abundant environments in high-pH conditions (Fig. 4a, b)[51,52]. The formed H^+ could stably accumulate on the local cathode surface. To distinguish the type of dissociated H_2O, we analyzed the envelope peaks at 3000-3700 cm⁻¹ which can be deconvoluted into three types of interfacial H_2O, including tetra-hedrally coordinated water (tetra-H_2O, 3230 cm⁻¹), trihedrally coordinated water (tri-H_2O, 3450 cm⁻¹) and dangling O-H bonds of water (dangling O-H, 3600 cm⁻¹), respectively[36,48,50]. The three types of interfacial water can vary as a function of electrode potential due to the Stark effect. At more negative potentials, the changes in peak intensity and shift of these interfacial water would accordingly become obvious. Compared to the tetra-H_2O and tri-H_2O, dangling O-H water exhibited a smoother area change and a steeper shift slope (−23.0 cm⁻¹ V⁻¹) as the potential decreases (Fig. 4c–e), certifying the preferential dissociation of dangling O-H water on Pd-Cl/Cu_2O. Although rapid dissociation of dangling O-H water also occurred over Pd/Cu_2O (Supplementary Figs. 26, 27), the non-detected H_3O^+ peaks suggested the difficulty in donating H^+ (Supplementary Fig. 26a), due to the strong binding of *H on Pd without Cl mediation. In addition, the inapparent shift of H_2O peak (1617 cm⁻¹) and the negligible H_3O^+ peak manifested the poor H_2O dissociation with little H^+ coverage on Cu_2O (Supplementary Fig. 28). Therefore, under the mediation of Cl, Pd-Cl/Cu_2O catalysts could promote dangling O-H water dissociation to construct the local H^+-abundant environments in alkaline conditions.

To validate the effective H^+ for *NO intermediates hydrogenation in alkaline NO_3RR over catalysts, in situ ATR-IR was carried out (Supplementary Figs. 29–31). Under the driven of applied potential from 0.2 to −0.7 V vs. RHE, the detected N-O peaks (at 1540 cm⁻¹)[53] in the spectra of Pd-Cl/Cu_2O demonstrated the deoxygenation of NO_3^- to the intermediate *NO. The conspicuous peaks of hydro-nitrogen intermediates (-NH) at 3200−3380 cm⁻¹ indicated the effective hydrogenation of *NO intermediates on Pd-Cl/Cu_2O[54–57]. In comparison, Pd/Cu_2O displayed the stronger *NO intermediate peaks and the weaker

-NH signals (Fig. 4f, g). These results evidenced that Cl-mediated H^+ feeding could boost *NO intermediates hydrogenation in alkaline NO_3RR for promising NH_3 synthesis over Pd-Cl/Cu_2O.

Alkaline NO₃RR performance

The electrocatalytic NO_3RR performance was conducted under ambient temperature and pressure in a standard three-electrode H-type cell. NH_4^+, NO_3^-, and NO_2^- in the reaction system were detected and quantified by colouration and ¹H nuclear magnetic resonance (NMR) experiments (Supplementary Figs. 32−36). Given the common industrial and agricultural wastewater-relevant NO_3^- concentration ranging from 40 to 80 mM[58–61], we reasonably selected 56 mM NO_3^- in the electrolyte (pH = 14) for the standard electrochemical tests. Linear sweep voltammetry (Supplementary Fig. 37) curves of Pd-Cl/Cu_2O presented the distinct cathodic reduction peak between 0 and −0.5 V vs. RHE in the NO_3^--containing electrolyte relative to NO_3^--free solutions, expressing the underlying NO_3RR process. The NO_3RR performance was then determined by chronoamperometry (Supplementary Fig. 38). Pd-Cl/Cu_2O delivered an excellent NH_3 yield rate of 30.1 mg h⁻¹ cm⁻² with a corresponding NH_3 FE of 99.2% and a current density of 350 mA cm⁻² at −0.4 V vs. RHE (Fig. 5a and Supplementary Fig. 38c), in which the NH_3 yield rate value was 5-folds and 2.1-folds than that of Cu_2O and Pd/Cu_2O. The electrochemical surface area-normalized NH_3 yield also verified the best internal activity of Pd-Cl/Cu_2O (Supplementary Fig. 39, 40).

The KIE experiment which used D_2O solvent for replacing the H_2O in the electrolyte was tested to further investigate the NO_3RR performance (Fig. 5b and Supplementary Fig. 41)[62,63]. The Cu_2O presented a higher KIE value (ratio of NH_3 yield rate in H_2O to D_2O) of 2.3, elucidating that the sluggish H_2O dissociation limited the H^+ offer to hinder NH_3 activity. After introducing Pd SACs, the sharply decreased KIE over Pd/Cu_2O (1.23) and Pd-Cl/Cu_2O (1.05) corroborated the accelerated H_2O dissociation, matching with the in situ Raman results. While, the lower NH_3 yield rate of Pd/Cu_2O than that of Pd-Cl/Cu_2O resulted from
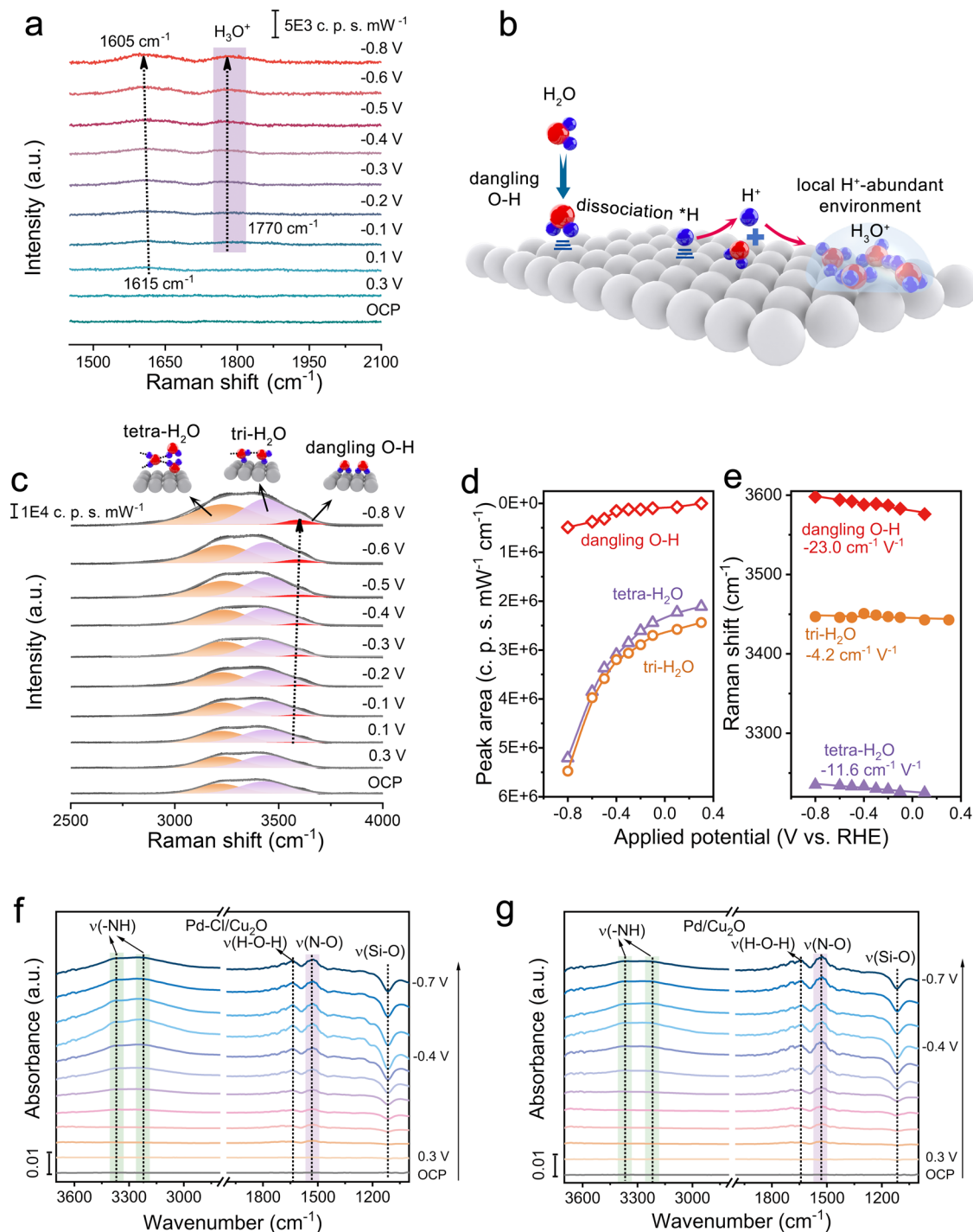
Fig. 4 | NO₃⁻ intermediates hydrogenation. a In situ Raman spectra of Pd-Cl/Cu₂O.
b Schematic diagram of the local H⁺-abundant environment construction over Pd-Cl/Cu₂O. In situ Raman spectra of Pd-Cl/Cu₂O (**c**), corresponding peak area (**d**) and

Raman shift (**e**) of various interfacial H₂O structures. In situ ATR-IR spectra of Pd-Cl/Cu₂O (**f**) and Pd/Cu₂O (**g**) catalysts. Si-O signal was derived from the reduction of surface SiO₂ on the Si semi-cylindrical prism substrate under the applied potentials.

the strong binding of *H on Pd, which induced the side reaction of hydrogen-hydrogen dimerization (Supplementary Figs. 41, 42). Under the Cl-mediated H⁺ feeding effect, Pd-Cl/Cu₂O obtained superior alkaline NO₃RR performance. Control experiments further demonstrated that the mediated effect originated from the Cl ligand of Pd-Cl/Cu₂O rather than the free Cl ions in the system (Supplementary Figs. 43, 44).

The NO₃⁻ removal ability over the catalysts was examined by carrying out conversion tests under 56 mM NO₃⁻ at −0.4 V vs. RHE. The three catalysts, Pd-Cl/Cu₂O, Pd/Cu₂O and Cu₂O, all showed a high NO₃⁻

conversion rate of ~99%, indicating that Cu₂O matrix has a strong NO₃⁻ removal ability. Yet, the NO₃⁻ to NH₃ conversion rates of Cu₂O and Pd/Cu₂O within 1 h electrolysis were as low as ~20% and ~45%, respectively, accompanied by producing 26% and 21% of NO₂⁻ (Supplementary Fig. 45). Electrochemical online differential electrochemical mass spectrometry (DEMS) showed that Cu₂O and Pd/Cu₂O also generated the gas products during the potentiostatic process at −0.4 V vs. RHE (Supplementary Fig. 46a, b), including the m/z signals of NH₃ (17), H₂ (2), N₂ (28), NO (30), NH₂OH (33), and N₂O (44). Notably, nearly all the NO₃⁻ was converted into NH₃ on Pd-Cl/Cu₂O within 1 h electrolysis, and
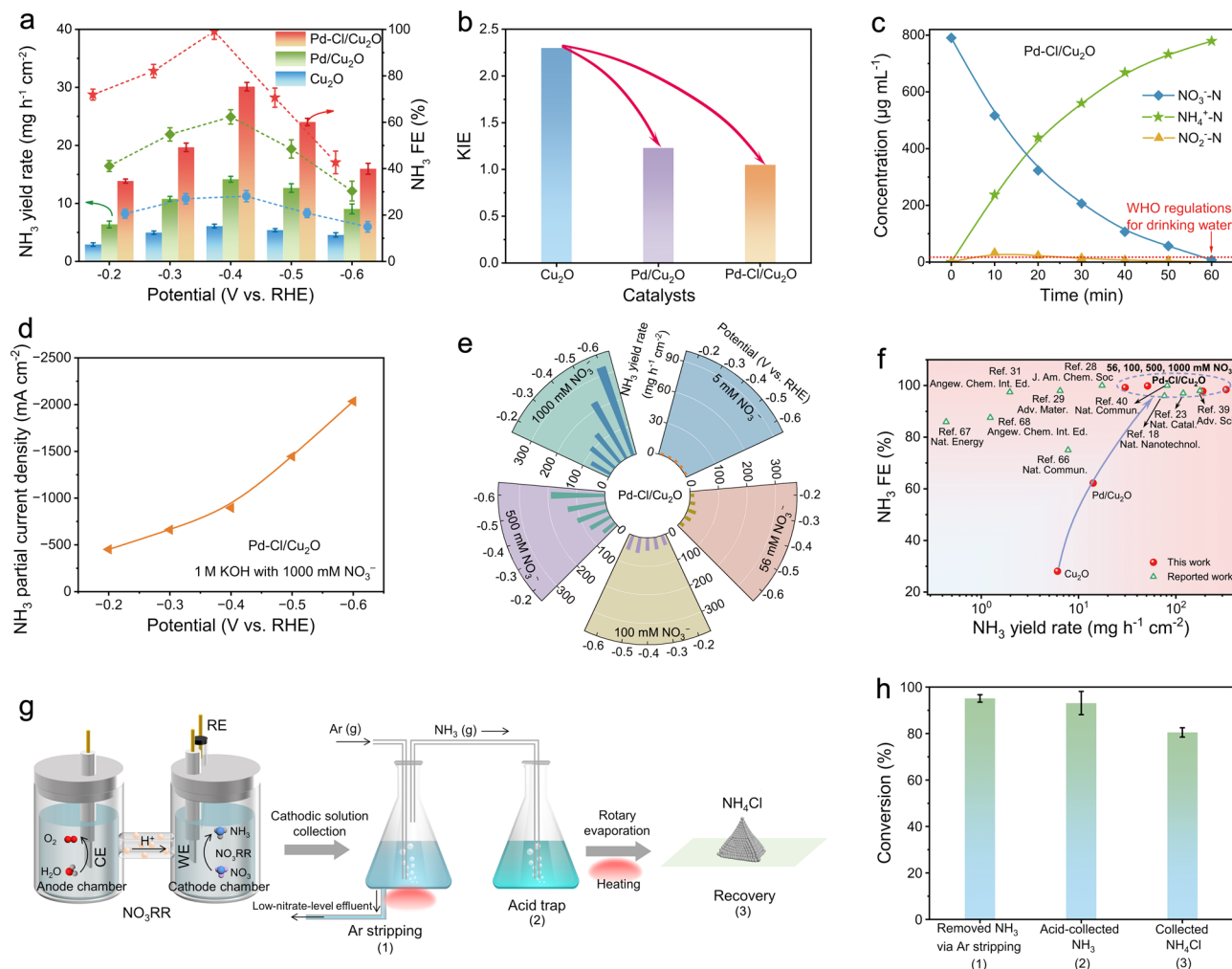
Fig. 5 | Alkaline NO₃RR performance. a NH₃ yield rate and NH₃ FE of catalysts in a 1 M KOH with 56 mM NO_3^- electrolyte (pH = 14) for 1 h electrolysis. Catalyst mass loading: 3 mg cm⁻². Resistance of catalyst: 0.156 Ω cm⁻². Resistance of electrolyte: 1.45 Ω. **b** Kinetic isotopic effect (KIE) diagram for the ratio of NH₃ yield rate in H₂O to D₂O solvent in a 1 M KOH with 56 mM NO_3^- electrolyte at −0.4 V vs. RHE. **c** NO_3^- removal of catalysts measured in a 1 M KOH with 56 mM NO_3^- electrolyte (equals 790.3 μg mL⁻¹ NO_3^-–N) at −0.4 V vs. RHE. After 1 h electrolysis, only 7.1 μg mL⁻¹ of NO_3^-–N and 0.85 μg mL⁻¹ of NO_2^-–N remained, both below the WHO regulations for drinking water (NO_3^-–N < 11.3 μg mL⁻¹ and NO_2^-–N < 0.91 μg mL⁻¹). **d** NH₃ partial current densities of Pd-Cl/Cu₂O in a 1 M KOH electrolyte with 1000 mM NO_3^- under the potential range from −0.2 to −0.6 V vs. RHE. **e** NH₃ yield rate of Pd-Cl/Cu₂O in a 1 M KOH electrolyte with different NO_3^- concentrations for 1 h of electrolysis. **f** NO₃RR performance comparison of reported electrocatalysts. **g** Schematic of the ammonia product synthesis process from 1000 mM NO_3^- electrolyte to NH₄Cl for 5 h electrolysis at −0.6 V vs. RHE. **h** The conversion efficiency of different steps for the ammonia product synthesis process. Numbers on the *x*-axis indicated the corresponding conversion steps in panel **g**. Error bars indicate the relative standard deviations of the mean (*n* = 3). See "Methods" for experimental details.

the corresponding selectivity reached ~99.1% with negligible NO_2^- and gas products (Fig. 5c and Supplementary Fig. 46c). The residual NO_3^- and NO_2^- concentrations were both significantly lower than the World Health Organization (WHO) regulations for drinking water (Supplementary Fig. 47)[64,65]. These results corroborated the excellent NO_3^- removal rate and high NH₃ selectivity of Pd-Cl/Cu₂O. In addition, Pd-Cl/Cu₂O behaved with favorable NO₃RR stability during ten-cycling tests (Supplementary Fig. 48). The morphology, phase structure, chemical valence state, atomic coordination environment and electrochemical properties remained steady after the electrolysis, further indicating the robust structure of catalysts (Supplementary Figs. 49–52 and Supplementary Tables 3, 4).

Furthermore, the optimal Pd-Cl/Cu₂O (Supplementary Table 5 and Supplementary Figs. 53, 54) was utilized to explore the NO₃RR performance at different NO_3^- concentrations, due to the diverse pollutant sources with a broad scope of NO_3^- concentrations[1,66]. Aside from 56 mM NO_3^-, 5, 100, 500, and 1000 mM NO_3^- were also chosen to cover the concentration range expected in household and

heavy-industry wastewater (Supplementary Fig. 55, 56). The catalyst not only exhibited an excellent NH₃ FE (~97.8%) in 5 mM NO_3^- system (Supplementary Fig. 57), but also preserved the high NH₃ selectivity of >95% under higher NO_3^- concentration (100-1000 mM). Impressively, Pd-Cl/Cu₂O achieved an industrial-relevant NH₃ partial current density of ~2 A cm⁻² (Fig. 5d) while maintaining 99.1% NH₃ FE, with a splendid NH₃ yield rate of ~330 mg h⁻¹ cm⁻² at 1000 mM NO_3^- concentration systems (Fig. 5e), which outperformed almost all state-of-the-art NO₃RR performance ever reported (Fig. 5f and Supplementary Table 6)[18,23,28,29,31,40,66–68].

With the impressive NO₃RR performance of Pd-Cl/Cu₂O catalyst, the high-purity ammonia products were collected to demonstrate their practical application potential (Fig. 5g). After conducting NO₃RR tests in a sealed reactor, the cathodic electrolyte was transferred into a conical flask. The generated NH₃ was striped at 70 °C by an Ar stripping method owing to the high NH₃ vapor pressure in the alkaline environment (see details in Methods)[69,70]. As a result, ~95.2% of the NH₃ vapor was successfully stripped out from the electrolyte (Fig. 5h),

indicating water source denitrification with high efficiency and simultaneous production of high value-added NH_3. The outflowing NH_3 gas was trapped in a HCl solution (~93.1%), subsequently performed rotary evaporation, and finally collected ~80.5% of NH_4Cl powder. While the high-purity NH_4Cl powder (confirmed by XRD measurement in Supplementary Fig. 58) sheds light on the potential as a fertilizer for agricultural production, the limitations induced by additional cost of nitride concentration, interference (such as heavy metals and CODs) removal and product recovery[17] needs to be considered and overcome for practical ammonia products.

In addition to Cl mediated strategy, this performing principle with high NH_3 performance was available for other halogen ligand systems, such as Pd-F/Cu_2O, Pd-Br/Cu_2O and Pd-I/Cu_2O. These catalysts were successfully synthesized using a similar wet-immersion and H_2 calcination approach, as proved by XRD and XPS characterization (Supplementary Figs. 59–62). Besides, Pd-(F, Br, I)/Cu_2O catalyst exhibited a higher NH_3 activity and selectivity for alkaline NO_3RR than those of Cu_2O matrix and Pd/Cu_2O. Their NH_3 yield rates in a 1 M KOH with 56 mM NO_3^- electrolyte at −0.4 V vs. RHE were ~3.7, ~3.1, ~2.6-fold of Cu_2O, and ~1.7, ~1.4, ~1.2-fold of Pd/Cu_2O, respectively (Supplementary Fig. 63a). The corresponding NH_3 FE value were ~2.9, ~2.3, ~2.1-fold of Cu_2O, and ~1.3, ~1.2, ~1.1-fold of Pd/Cu_2O, respectively (Supplementary Fig. 63b). Therefore, halogen-mediate strategy has expansive universality in enhancing alkaline NO_3RR performance.

In summary, we have proposed and realized a highly efficient halogen-mediated H^+ feeding strategy to boost the NO_3RR to NH_3 synthesis in alkaline conditions. Nitrate reduction to NH_3, instead of N_2, significantly enhances the product value of the electrochemical process. NH_3 can serve as a valuable nitrogen source in agricultural fertilizers, a chemical feedstock for various industrial processes, and a high-energy-density carrier for renewable hydrogen. The optimal Pd-Cl/Cu_2O nanocrystals achieved a NH_3 partial current density of ~2 A cm^{-2} while maintaining a nearly 100% NH_3 FE with a high NH_3 yield rate of ~330 mg h^{-1} cm^{-2} at 1 M NO_3^- concentration (pH = 14). Our platform displayed an over 99.1% NO_3^--to-NH_3 conversion efficiency from a typical industrial wastewater level to a drinkable water level. Further, it delivered a conversion of NO_3^- into practical NH_4Cl products with near-unity efficiency. Through a combination of theoretical simulations, in situ Raman, in situ ATR-IR, and KIE experiments, we have gained insights into the underlying mechanisms responsible for such highly selective and active NH_3 synthesis over Pd-Cl/Cu_2O. The presents of Cl ligand induced a prominent shift in the d-band center of Pd atoms, facilitating dangling O-H water dissociation and fast *H desorption. The constructed local H^+-abundant environments supported the free H^+ feeding to *NO intermediate hydrogenation, and thus realizing efficient NO_3^--to-NH_3 conversion. The success of the halogen-mediated strategy presented in this study paves the way for the utilization of other halogen elements, such as F, Br, and I, in Pd-(F, Br, I)/Cu_2O catalyst systems for alkaline NO_3RR to NH_3. The broader applicability of this approach demonstrates its potential for achieving sustainable NH_3 synthesis in alkaline conditions and inspiring innovated design of environmentally friendly technologies in the field of water treatment and environmental remediation.

Methods
Chemicals
Salicylic acid ($C_7H_6O_3$), trisodium citrate dihydrate ($Na_3C_6H_5O_7 \cdot 2H_2O$), sodium hydroxide (NaOH), sodium hypochlorite (NaClO), hydrochloric acid (HCl, 38%), potassium nitrate ($^{14}KNO_3$), potassium nitrite (KNO_2), potassium iodide (KI), and ethanol (C_2H_6O) were purchased from Sinopharm Chemical Reagent Co., Ltd. Sulfanilamide ($C_6H_8N_2O_2S$), p-dimethylaminobenzaldehyde (PDAB), sodium nitroferricyanide (III) dihydrate ($Na_2Fe(CN)_5NO \cdot 2H_2O$), N-(1-Naphthyl)

ethylenediamine dihydrochloride ($C_{12}H_{14}N_2 \cdot 2HCl$), potassium hydroxide (KOH), potassium nitrate ($^{15}KNO_3$), dimethyl sulfoxide (DMSO-$d6$), maleic acid ($C_4H_4O_4$), ammonium chloride ($^{14}NH_4Cl$, $^{15}NH_4Cl$), palladium chloride ($PdCl_2$), palladium diacetylacetonate ($Pd(O_2CCH_3)_2$), palladium oxide (PdO), palladium bromide ($PdBr_2$), palladium nitrate $Pd(NO_3)_2$, and palladium(II) trifluoroacetate ($Pd(O_2CCF_3)_2$) were purchased from Aldrich Chemical Reagent Co., Ltd. All reagents were analytical reagent grades and used as received without further purification. The water used in this research was purified through a Millipore system.

Preparation of Cu_2O
In a typical procedure, Cu foam (10 × 15 × 0.5 mm^3) was ultrasonically washed with acetone, 2 M HCl, ultrapure water and ethanol to clean the surface, respectively. The dried pre-treated Cu foam was then anodized in a 3 M KOH solution to form the blue $Cu(OH)_2$ nanowires by galvanostatic deposition at 20 mA cm^{-2} for 900 s. The brick red lotus-like Cu_2O was synthesized by annealing $Cu(OH)_2$ nanowires in a tube furnace at 550 °C for 2 h in N_2 atmosphere. The Cu_2O substrate plays a dual role in the catalysis. On one hand, it effectively facilitates the adsorption, activation and conversion of nitrate. On the other hand, it serves as a platform for loading Cl-coordinated Pd single atoms and provides Cu active sites to boost the NO_3RR process.

Preparation of Pd-Cl/Cu_2O
A certain amount of 0.03 M $PdCl_2$ solution was immersed into the Cu foam-supported lotus-like Cu_2O (10 × 10 mm^2), followed by reduction at 170 °C for 15 min in 10% H_2/Ar atmosphere to obtain the Pd-Cl/Cu_2O catalyst. Pd-Cl/Cu_2O catalysts with various Pd loadings were prepared according to the above procedure by changing the additional amount of $PdCl_2$ solution. The Cl acted as a synthetic directing agent to stabilize Pd single atoms.

Preparation of Pd/Cu_2O
A certain volume of 0.03 M $Pd(O_2CCH_3)_2$ solution was soaked into the Cu foam-supported lotus-like Cu_2O (10 × 10 mm^2), followed by reduction at 250 °C for 15 min in 10% H_2/Ar atmosphere to obtain the Pd/Cu_2O catalyst.

Preparation of Pd-F/Cu_2O, Pd-Br/Cu_2O and Pd-I/Cu_2O
For the synthesis of Pd-F/Cu_2O, a certain amount of 0.03 M $Pd(O_2CCF_3)_2$ was dropped into the Cu foam-supported lotus-like Cu_2O (10 × 10 mm^2), followed by heating at 250 °C for 15 min in 10% H_2/Ar atmosphere. The Pd-Br/Cu_2O or Pd-I/Cu_2O were synthesized under the same procedure except that $Pd(O_2CCF_3)_2$ was replaced by $PdBr_2$ or $Pd(NO_3)_2$ and KI.

Electrochemical testing
Before the NO_3RR tests, Nafion 117 membrane was pretreated as followed: first oxidizing in 5% H_2O_2 solution at 80 °C for 1 h to eliminate organic impurities, next boiling in deionized (DI) water for 1 h to clean the redundant H_2O_2 and reach the expansion, then using 0.5 M H_2SO_4 at 80 °C for 1 h to remove metallic impurities and residual ammonia contaminations and to protonate the membrane, finally operating DI water to rinse the excess acid and further expand the Nafion 117. The procedure should be repeated at least every 3 days to reuse the membrane.

The NO_3RR was measured on an electrochemical workstation (PARSTAT 4000) with a three-electrode system in a typical H-type cell, including as-prepared catalyst electrodes (working electrode, WE), platinum electrode (counter electrode, CE), and a saturated calomel electrode (reference electrode, RE). Nafion 117 membrane was fixed between the anode and cathode cells, and each cell contained 32 mL of 1 M KOH with 56 mM NO_3^- electrolyte). All potentials reported in this

work were referred to RHE scale via calibration by the following equation: E(vs. RHE) = E(vs. SCE) + 0.244 + 0.0591 × pHvalue. The theoretical potential for nitrate reduction to ammonia was 0.69 V vs. RHE at pH = 14[30,71]. The error bars were the relative standard deviations obtained by at least three repeated tests. The CV-activation before reaction was conducted to remove impurities on the electrode surface. For the chronoamperometry measurement, the potential was applied from −0.2 to −0.6 vs. RHE. LSV was carried out in a voltage window from 0.2 to −1.0 V vs. RHE at scan rates of 10 mV·s^{-1}.

Detection and quantification of NH$_3$ using UV-vis

The concentration of NH$_3$ was spectrophotometrically detected by the salicylic acid method[72]. In detail, the electrolyte from the cathode cell was collected and diluted to the detection range. Then, 2 mL of diluted sample was mixed with 2 mL of 1 M NaOH solution containing 5 wt% salicylic acid and 5 wt% sodium citrate. Subsequently, 1 mL of 0.05 M NaClO and 0.2 mL of $C_5FeN_6Na_2O$ solution (1 wt%) were added to the mixture component and shaken well. After stewing for 2 h, UV-vis spectrophotometer measurements were performed with the range from 500 to 800 nm and recorded the absorbance at the wavelength of 655 nm. The concentration-absorbance curve was calibrated using standard NH$_4$Cl solution with concentrations of 0.1, 0.5, 1.0, 2.0, 3.0, 5.0 and 10.0 μg mL^{-1} in 1 M KOH with NO$_3^-$. And the fitting curve ($y = 0.104x - 0.014$, $R^2 = 0.999$) displayed a good linear relation of absorbance value with NH$_4^+$ concentration.

Detection and quantification of NO$_3^-$ using UV-vis

The electrolyte from the cathode cell was collected and diluted to the detection range. 5 mL of diluted sample solution was mixed with 0.1 mL of 1 M HCl. After stewing for 20 min, the UV-vis absorbance at the wavelength ranging from 215 to 280 nm was detected[73,74]. The intensities at wavelengths of 220 and 275 nm were recorded, and the final absorbance difference was calculated using the equation: $A = A_{220\,nm} - A_{275\,nm}$. The concentration-absorbance difference curve was calibrated using standard KNO$_3$ solution with 5, 10, 15, 20, 25, 30 and 50 μg mL^{-1} concentrations. And the fitting curve ($y = 0.051x + 0.013$, $R^2 = 0.999$) displayed a good linear relation of absorbance value with NO$_3^-$ concentration.

Detection and quantification of NO$_2^-$ using UV-vis

The configuration of color reagent was as follows[73,74]: First, 0.5 g of sulfonamide was dissolved in 50 mL of 2.0 M HCl solution, which was marked as reagent A. Then, 20 mg of N-(1-naphthyl) ethylenediamine dihydrochloride was dispersed in 20 mL of DI water, which was denoted as reagent B. Subsequently, 0.1 mL of reagent A was dropped into 5 mL of standard or diluted sample solutions, mixing up and stewing for 10 min. Furthermore, 0.1 mL of reagent B was injected into the above solution, shaking up and resting for 30 min. The UV-vis absorbance at the wavelength ranging from 400 to 640 nm was recorded, in which the typical absorption peak of NO$_2^-$ was located at 540 nm. The concentration-absorbance difference curve was calibrated using standard KNO$_2$ solution with concentrations of 0.05, 0.1, 0.2, 0.5, 1.0, 2.0 and 3.0 μg mL^{-1}. And the fitting curve ($y = 0.768x - 0.012$, $R^2 = 0.999$) displayed a good linear relation of absorbance value with NO$_2^-$ concentration.

Detection and quantification of NH$_3$ using ^{1}H NMR

To support the UV-vis results, ^{14}NO$_3^-$ and ^{15}NO$_3^-$ isotope labeling experiments were conducted on Bruker AVANCE III HD NMR spectrometer (600 MHz). The pH value of the diluted electrolyte after NO$_3$RR was adjusted to 2 with 1 M HCl. Then 0.5 mL of the above solutions was mixed with 0.1 mL DMSO-$d6$ with 0.04% $C_4H_4O_4$, which served as a solvent and maleic acid $C_4H_4O_4$ as the internal standard. ^{1}H NMR was recorded to quantitatively analyze of NH$_3$ product according to the corresponding standard curves.

Electrochemical in situ Raman spectroscopy

In situ Raman was tested by inVia Reflex (Renishaw, UK) with a 633 nm laser as the excitation source. The NO$_3$RR was performed in the custom-made Teflon reactor with a quartz window, in which the Ag/AgCl (Supplementary Fig. 25), Pt wire, and catalysts coated on Au electrode were used for the reference, counter, and working electrode, respectively. In situ Raman spectra were recorded in electrolytes with NO$_3^-$ by the potential from open circuit potential (OCP) to −0.8 V vs. RHE.

Electrochemical in situ ATR-IR spectroscopy

ATR-IR was measured on a Nicolet iS50 FT-IR spectrometer equipped with an MCT detector and cooled by liquid nitrogen during the electrochemical process (Supplementary Fig. 29). The NO$_3$RR was performed in the custom-made reactor with three-electrode, in which the Ag/AgCl and Pt wire were used for the reference and counter electrode, respectively. The working electrode was prepared as followed: First, the Si semi-cylindrical prism was polished with Al$_2$O$_3$ powder and sonicated in acetone and deionized water. The Si was pretreated in a piranha solution at 60 °C for 20 min to clean the organic contaminants. Then the reflecting surface of Si was plated in the Au precursor mixture at 60 °C for 10 min, obtaining the Au-coated Si (20 mm in diameter) conductive substrate. Finally, the catalyst ink was dropped on the substrate reflecting surface for employment in the reaction. In situ ATR-IR spectra were recorded in electrolyte with NO$_3^-$ by the potential from 0.3 V to −0.7 V vs. RHE. The spectrum collected at OCP was used for background subtraction.

Electrochemical online DEMS tests

The online DEMS tests were performed in customized reactors containing 1 M KOH with 56 mM NO$_3^-$ electrolyte. Ar was continuously bubbled into the electrolyte. Catalysts coated on breathable film with gold plating layer, Pt wire, and saturated Ag/AgCl electrode were used as the working, the counter and the reference electrode, respectively. After the baseline of the mass spectrometry kept steady, the potential of OCP and −0.4 V vs. RHE were applied alternately with an interval of 3 min. Accordingly, the differential mass signals appeared when the gaseous products formed on the electrode surface. The mass signal returned to baseline after the electrochemical measurement was over. To avoid accidental errors, the next cycle started using the same conditions. After five cycles, the experiment was ended.

Direct ammonia product synthesis

To evaluate the NH$_3$ removal efficiency via Ar stripping and the NH$_3$ collection efficiency by acid trap, 50 mL of cathodic electrolyte after NO$_3$RR test was sealed in a conical flask at 70 °C and flowed in 100 sccm Ar gas for 5 h to perform the Ar stripping to purge the NH$_3$ gas out. The outlet gas stream was meanwhile purged into 50 mL of 2 M HCl to collect the NH$_3$ product. The amount of NH$_3$ in all the solutions was measured by the salicylic acid method mentioned above, and the removal efficiency and collection efficiency were calculated as following equations, respectively:

$$\text{Removed NH}_3 \text{ via Ar stripping} = 1 - \frac{\text{NH}_3 \text{ left after Ar stripping (mol)}}{\text{initial NH}_3 \text{ (mol)}}$$

$$\text{(1)}$$

$$\text{Acid collected NH}_3 = \frac{\text{NH}_3 \text{ in acid trap (mol)}}{\text{removed NH}_3 \text{ via Ar } stripping \text{ (mol)}} \quad \text{(2)}$$

To produce the NH$_4$Cl product and estimate the production efficiency, the 50 mL of HCl with the trapped NH$_3$ was dried by rotary evaporator at 70 °C in an oven overnight. The final NH$_4$Cl was measured by a balance and analyzed by XRD. The collection efficiency of

NH_4Cl from the acid trap was calculated by following equation:

$$\text{Collected } NH_4\,Cl \text{ from acid trap} = \frac{\text{collected dried out } NH_4\,Cl\,(mol)}{\text{acid collected } NH_3\,(mol)} \tag{3}$$

DFT computational details

All calculations were carried out by spin-polarized DFT with the Vienna Ab initio Simulation Package (VASP)[75,76]. Electron exchange-correlation was expressed by the Perdew–Burke–Ernzerhof (PBE) functional within the generalized gradient approximation (GGA)[77]. To describe the ionic cores, the projector augmented wave (PAW) pseudopotential was applied[78,79]. The Monkhorst–Pack K-points were set to be $2 \times 2 \times 1$ for geometry optimization and density of states (DOS) calculations. The plane wave energy cutoff, and convergence criterion for electronic energy and forces were set as 450 eV, 10^{-5} eV, and 0.02 eV/Å, respectively (Supplementary Fig. 64). A vacuum layer of 15 Å was adopted in the models[80]. Aqueous phase H_2O and NO_3^- were as the energetics references.

Cu$_2$O with crystal planes (111) was modeled with a periodic 4-layer, where the lower two layers were fixed and the upper two layers were relaxed. The model included 64 Cu atoms and 32 O atoms. The optimized lattice constants were a = 12.09 Å and b = 10.47 Å, the thickness of this model was 8.79 Å. The computational hydrogen electrode (CHE) model was used to calculate the change in Gibbs free energy (ΔG)[81]. In CHE model, $H^+ + e^- \rightleftharpoons 1/2\,H_2(g)$ was equilibrated at 0 V vs. the reversible hydrogen electrode (RHE) at all pH values.

Constant-potential calculations were applied using the code freely available from Duan and Xiao[82]. At the applied potential (U) on the standard hydrogen electrode (SHE) scale, the number of electrons and the atomic coordinates of the system are optimized simultaneously. The chemical potential of the electron ($\bar{\mu}_e$) is calculated as

$$\mu e = \mu e, SHE + U \tag{4}$$

where $\mu_{e,SHE}$ is the electronic chemical potential of the system relative to the SHE.

$$\mu e, SHE = E_f/e - Vsol + \varphi 0/e \tag{5}$$

where E_f is the Fermi level, V_{sol} is the potential deep in the solution, and $\varphi_O = -4.6$ eV for the SHE. The grand canonical energy of the system is defined as

$$\Omega = E_{DFT} + \Delta n \cdot (U - V_{sol} + \varphi_0/e) \tag{6}$$

where E_{DFT} is the energy calculated from the DFT and Δn is the number of electrons added or removed from the system.

The chemical potential of the electron ($\bar{\mu}_e$) is derived as

$$\bar{\mu}_e = \partial \Omega/\partial n = E_f/e - V_{sol} + \varphi_0/e + U \tag{7}$$

where Ω is the grand canonical energy.

Calculation of thermodynamic corrections

The zero-point energy for each species is calculate by

$$E_{ZPE} = \sum_i \frac{h v_i}{2} \tag{8}$$

where v_i is the vibration frequency. The entropy contributions of translational, rotational, vibrational, and electronic motion can be calculated by

$$S_t = R\left\{ \ln\left[\left(\frac{2\pi m k_B T}{h^2} \right)^{3/2} \frac{k_B T}{P} \right] + \frac{5}{2} \right\} \tag{9}$$

$$S_r = R\left[\ln\left(\frac{T}{\sigma_r} * \frac{8\pi^2 I k_B}{h^2} \right) + 1 \right] \tag{10}$$

$$S_v = R\sum_i \left\{ \frac{h v_i}{k_B T} \frac{e^{-\frac{h v_i}{k_B T}}}{1 - e^{-\frac{h v_i}{k_B T}}} - \ln\left[1 - e^{-\frac{h v_i}{k_B T}} \right] \right\} \tag{11}$$

$$S_e = R * \ln(N + 1) \tag{12}$$

where N is the number of unpaired electrons, R is the gas constant, P is the pressure, k_B is the Boltzmann constant[83].

From the above formula, considering that the vibration frequency of the catalyst substrate is small, its corresponding correction is very small and does not affect the calculation results. Thus, we mainly made corrections to gas molecules and adsorbents on the catalyst, and entropic effects of the catalyst substrate would not be considered further.

H_2O as the proton source in alkaline conditions. The pH has an influence on the major proton donor in the research system. For alkaline nitrate reaction pathways (pH = 14), we have considered H_2O as the proton source. Under this condition, the H* path will be through the alkaline pathway.

$$H_2O + e^- + * \rightarrow H_2O^* + e^- \rightarrow H^* + OH^- \rightarrow 1/2H_2 + OH^- + * \tag{13}$$
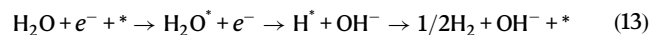
$$G_{OH^-} - G_{H_2O} - G_{e^-} = G_{1/2H_2} - eU_{RHE} \tag{14}$$

For electrochemical steps in nitrate reduction, the free energy changes are calculated using the products and reactants of the following reaction equation:

$$H_2O + X^* + e^- \rightarrow XH^* + OH^- \tag{15}$$
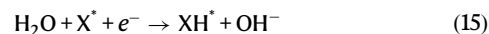
$$\Delta G(U) = G_{XH^*} - G_{X^*} + G_{OH^-} - G_{H_2O} - G_{e^-} = G_{XH^*} - G_{X^*} + G_{1/2H_2} - eU_{RHE} \tag{16}$$

The calculation method for pH and potential effects. The free energies of adsorption of ionic species are calculated using thermodynamic Hess cycles, which cycles include the effects of entropy, solvation energy, protonation energy (including pH effects) and potential effects. The Gibbs energy formulas for nitrate reduction reaction steps are reported by Muhich et al.[16,18,84]. The method is based on that of Calle-Vallejo et al.[85] and Liu et al.[86]. The free energy of anion A$^-$ is calculated according to:

$$A^- + * \leftrightarrow A^* + e^- \tag{17}$$

$$\Delta G_{ads}(A^-) = E_{A^*} + [G_{H^+} + G_{e^-}] - [G_{HA} - \Delta G_{sol} - \Delta G_{protonation}] - E^* \tag{18}$$

Where E_* and E_{A^*} are the DFT computed enthalpies of bare surface and A* adsorbed to the surface, respectively. G_{H_2} and G_{HA} are the Gibbs free energies of desorbed species H_2 and HA, respectively, in the gas

phase at 300 K, as calculated from the following:

$$G_{HA} = E_{HA} + E_{ZPE} - T^*S \qquad (19)$$

where E_{HA} is the DFT computed energy of HA in the gas phase, T is the temperature (300 K), E_{ZPE} is the contribution of the zero-point energy, S is the entropic contributions to the free energy obtained using the JANAF database. The solvation energy is described:

$$\Delta G_{sol} = G_{HA(g)} - G_{HA(l)} \qquad (20)$$

The pH accounts for the effects on the free energies of the species. Free energy modifications due to pH were calculated according to:

$$\Delta G_{protonation} = G^{O} - 2.303kT(pK_a - pH) = G_{A^-} + G_{H^+} - G_{HA(l)}$$
$$- 2.303kT(pK_a - pH) \qquad (21)$$

$G_{HA(g)}$ and $G_{HA(l)}$ are the free energies of HA molecule in the gas and liquid phases respectively. k is the Boltzmann constant. K_a is the acid dissociation constant for the A^- anion. The standard state (25 °C, 100 kPa, 1 mol/kg) energies of ion and neutral species in aqueous solution ($G_{HA(g)}, G_{HA(l)}, G_{A^-}, G_{H^+}, K_a$) are taken from the CRC handbook.

The computational hydrogen electrode (CHE) is used to account for potential effects on reaction energies[87]:

$$\Delta G = \Delta E + \Delta E_{ZPE} - T^*\Delta S + 0.0591^*pH - eU_{RHE} \qquad (22)$$

where ΔE is the DFT computed reaction (electronic) energy, ΔE_{ZPE} and ΔS are the zero-point energy difference and the entropy difference between the adsorbed state and the gas phase, respectively. 0.0591^*pH represents the free-energy contribution due to the variations in H concentration. We considered the effect of a potential bias on all states involving one electron or hole in the electrode by shifting the energy of this energy by eU_{RHE}, where U_{RHE} is the electrode potential relative to the reversible hydrogen electrode (RHE).

Data availability
All experimental data reported in this study and Supplementary Information are available from the corresponding author upon reasonable request.

References
1. Katsounaros, I., Dortsiou, M. & Kyriacou, G. Electrochemical reduction of nitrate and nitrite in simulated liquid nuclear wastes. *J. Hazard. Mater.* **171**, 323–327 (2009).
2. Burow, K. R., Nolan, B. T., Rupert, M. G. & Dubrovsky, N. M. Nitrate in groundwater of the united states, 1991–2003. *Environ. Sci. Technol.* **44**, 4988–4997 (2010).
3. Chen, J. G. et al. Beyond fossil fuel-driven nitrogen transformations. *Science* **360**, eaar6611 (2018).
4. Galloway, J. N. et al. Transformation of the nitrogen cycle: Recent trends, questions, and potential solutions. *Science* **320**, 889–892 (2008).
5. Smolders, A. J. P., Lucassen, E. C. H. E. T., Bobbink, R., Roelofs, J. G. M. & Lamers, L. P. M. How nitrate leaching from agricultural lands provokes phosphate eutrophication in groundwater fed wetlands: The sulphur bridge. *Biogeochemistry* **98**, 1–7 (2009).
6. Picetti, R. et al. Nitrate and nitrite contamination in drinking water and cancer risk: A systematic review with meta-analysis. *Environ. Res.* **210**, 112988 (2022).
7. Knobeloch, L., Salna, B., Hogan, A., Postle, J. & Anderson, H. Blue babies and nitrate-contaminated well water. *Environ. Health Persp.* **108**, 675–678 (2000).
8. Shrimali, M. & Singh, K. P. New methods of nitrate removal from water. *Environ. Pollut.* **112**, 351–359 (2001).
9. Rezvani, F., Sarrafzadeh, M. H., Ebrahimi, S. & Oh, H. M. Nitrate removal from drinking water with a focus on biological methods: A review. *Environ. Sci. Pollut. Res.* **26**, 1124–1141 (2019).
10. Meng, G. et al. NiFe layered double hydroxide nanosheet array for high-efficiency electrocatalytic reduction of nitric oxide to ammonia. *Chem. Commun.* **58**, 8097–8100 (2022).
11. Zhang, S. et al. Electrocatalytic reduction of NO to NH₃ in ionic liquids by P-doped TiO₂ nanotubes. *Front. Chem. Sci. Eng.* **17**, 726–734 (2023).
12. Zhang, W. et al. Single atomic cerium sites anchored on nitrogen-doped hollow carbon spheres for highly selective electroreduction of nitric oxide to ammonia. *J. Colloid Interface Sci.* **638**, 650–657 (2023).
13. Duca, M. & Koper, M. T. M. Powering denitrification: The perspectives of electrocatalytic nitrate reduction. *Energy Environ. Sci.* **5**, 9726 (2012).
14. Xu, H., Ma, Y., Chen, J., Zhang, W. X. & Yang, J. Electrocatalytic reduction of nitrate - a step towards a sustainable nitrogen cycle. *Chem. Soc. Rev.* **51**, 2710–2758 (2022).
15. Qi, D. et al. High-efficiency electrocatalytic NO reduction to NH₃ by nanoporous VN. *Nano Res. Energy* **1**, e9120022 (2022).
16. Wu, X. et al. Contrasting capability of single atom palladium for thermocatalytic versus electrocatalytic nitrate reduction reaction. *ACS Catal.* **13**, 6804–6812 (2023).
17. Van Langevelde, P. H., Katsounaros, I. & Koper, M. T. M. Electrocatalytic nitrate reduction for sustainable ammonia production. *Joule* **5**, 290–294 (2021).
18. Chen, F. Y. et al. Efficient conversion of low-concentration nitrate sources into ammonia on a Ru-dispersed Cu nanowire electrocatalyst. *Nat. Nanotechnol.* **17**, 759–767 (2022).
19. Liao, W. et al. Boosting nitrogen activation via Ag nanoneedle arrays for efficient ammonia synthesis. *ACS Nano* **17**, 411–420 (2023).
20. Liao, W. et al. Interfacial engineering promoting electrosynthesis of ammonia over Mo/phosphotungstic acid with high performance. *Adv. Funct. Mater.* **31**, 2009151 (2021).
21. Ding, J. et al. Iron-doping strategy promotes electroreduction of nitrate to ammonia on MoS₂ nanosheets. *Inorg. Chem. Commun.* **151**, 110621 (2023).
22. Dhamole, P. B., Nair, R. R., D'Souza, S. F. & Lele, S. S. Denitrification of highly alkaline nitrate waste using adapted sludge. *Appl. Biochem. Biotechnol.* **151**, 433–440 (2008).
23. Han, S. et al. Ultralow overpotential nitrate reduction to ammonia via a three-step relay mechanism. *Nat. Catal.* **6**, 402–414 (2023).
24. Gao, Q. et al. Breaking adsorption-energy scaling limitations of electrocatalytic nitrate reduction on intermetallic CuPd nanocubes by machine-learned insights. *Nat. Commun.* **13**, 2338 (2022).
25. Pérez-Gallent, E., Figueiredo, M. C., Katsounaros, I. & Koper, M. T. M. Electrocatalytic reduction of nitrate on copper single crystals in acidic and alkaline solutions. *Electrochim. Acta* **227**, 77–84 (2017).
26. Song, Z. et al. Efficient electroreduction of nitrate into ammonia at ultralow concentrations via an enrichment effect. *Adv. Mater.* **34**, e2204306 (2022).
27. Li, P., Jin, Z., Fang, Z. & Yu, G. A single-site iron catalyst with preoccupied active centers that achieves selective ammonia electrosynthesis from nitrate. *Energy Environ. Sci.* **14**, 3522–3531 (2021).
28. Li, J. et al. Efficient ammonia electrosynthesis from nitrate on strained ruthenium nanoclusters. *J. Am. Chem. Soc.* **142**, 7036–7046 (2020).
29. Gao, W. et al. Alloying of Cu with Ru enabling the relay catalysis for reduction of nitrate to ammonia. *Adv. Mater.* **35**, 2202952 (2023).

30. Wang, Y. et al. Enhanced nitrate-to-ammonia activity on copper-nickel alloys via tuning of intermediate adsorption. *J. Am. Chem. Soc.* **142**, 5702–5708 (2020).

31. Wang, Y. et al. Structurally disordered RuO_2 nanosheets with rich oxygen vacancies for enhanced nitrate electroreduction to ammonia. *Angew. Chem. Int. Ed.* **61**, e202202604 (2022).

32. Jiang, M. et al. Batch-scale synthesis of nanoparticle-agminated three-dimensional porous $Cu@Cu_2O$ microspheres for highly selective electrocatalysis of nitrate to ammonia. *Environ. Sci. Technol.* **56**, 10299–10307 (2022).

33. Yin, D. et al. Synergistic active phases of transition metal oxide heterostructures for highly efficient ammonia electrosynthesis. *Adv. Funct. Mater.* **33**, 2303803 (2023).

34. Hu, C., Zhang, L. & Gong, J. Recent progress made in the mechanism comprehension and design of electrocatalysts for alkaline water splitting. *Energy Environ. Sci.* **12**, 2620–2645 (2019).

35. Valenti, G. et al. Co-axial heterostructures integrating palladium/titanium dioxide with carbon nanotubes for efficient electrocatalytic hydrogen evolution. *Nat. Commun.* **7**, 13549 (2016).

36. Zhu, K. et al. Unraveling the role of interfacial water structure in electrochemical semihydrogenation of alkynes. *ACS Catal.* **12**, 4840–4847 (2022).

37. Li, Y. et al. Near-surface dilution of trace Pd atoms to facilitate Pd-H bond cleavage for giant enhancement of electrocatalytic hydrogen evolution. *Nano Energy* **34**, 306–312 (2017).

38. Zhang, T. et al. Pinpointing the axial ligand effect on platinum single-atom-catalyst towards efficient alkaline hydrogen evolution reaction. *Nat. Commun.* **13**, 6875 (2022).

39. Deng, X., Yang, Y., Wang, L., Fu, X. Z. & Luo, J. L. Metallic Co nanoarray catalyzes selective NH_3 production from electrochemical nitrate reduction at current densities exceeding 2 A cm^{-2}. *Adv. Sci.* **8**, 2004523 (2021).

40. Fang, J.-Y. et al. Ampere-level current density ammonia electrochemical synthesis using CuCo nanosheets simulating nitrite reductase bifunctional nature. *Nat. Commun.* **13**, 7899 (2022).

41. He, D. et al. Regulation of the electrocatalytic nitrogen cycle based on sequential proton–electron transfer. *Nat. Catal.* **5**, 798–806 (2022).

42. Koper, M. T. M. Theory of multiple proton–electron transfer reactions and its implications for electrocatalysis. *Chem. Sci.* **4**, 2710–2723 (2013).

43. Zhang, Y. et al. Photoelectrocatalytic reduction of CO_2 to syngas via SnO_x-enhanced Cu_2O nanowires photocathodes. *Adv. Funct. Mater.* **32**, 2109600 (2021).

44. Wang, Y., Zhou, W., Jia, R., Yu, Y. & Zhang, B. Unveiling the activity origin of a copper-based electrocatalyst for selective nitrate reduction to ammonia. *Angew. Chem. Int. Ed.* **59**, 5350–5354 (2020).

45. Du, P. et al. Single-atom-driven dynamic carburization over Pd_1–FeO_x catalyst boosting CO_2 conversion. *Chem* **8**, 3252–3262 (2022).

46. Han, Y. et al. Electronic structure engineering to boost oxygen reduction activity by controlling the coordination of the central metal. *Energy Environ. Sci.* **11**, 2348–2352 (2018).

47. Zhang, B. et al. Manganese acting as a high-performance heterogeneous electrocatalyst in carbon dioxide reduction. *Nat. Commun.* **10**, 2980 (2019).

48. Li, C.-Y. et al. In situ probing electrified interfacial water structures at atomically flat surfaces. *Nat. Mater.* **18**, 697–701 (2019).

49. Cai, C. et al. Atomically local electric field induced interface water reorientation for alkaline hydrogen evolution reaction. *Angew. Chem. Int. Ed.* **62**, e202300873 (2023).

50. Wang, Y. H. et al. In situ Raman spectroscopy reveals the structure and dissociation of interfacial water. *Nature* **600**, 81–85 (2021).

51. Wang, X., Xu, C., Jaroniec, M., Zheng, Y. & Qiao, S. Z. Anomalous hydrogen evolution behavior in high-pH environment induced by locally generated hydronium ions. *Nat. Commun.* **10**, 4876 (2019).

52. Tan, H. et al. Engineering a local acid-like environment in alkaline medium for efficient hydrogen evolution reaction. *Nat. Commun.* **13**, 2024 (2022).

53. Hu, B. & Li, J. One electron makes differences:From heme $\{FeNO\}^7$ to $\{FeNO\}^8$. *Angew. Chem. Int. Ed.* **54**, 10579–10582 (2015).

54. Yao, Y., Zhu, S., Wang, H., Li, H. & Shao, M. A spectroscopic study of electrochemical nitrogen and nitrate reduction on rhodium surfaces. *Angew. Chem. Int. Ed.* **59**, 10479–10483 (2020).

55. Wirz, R., Ferri, D. & Baiker, A. ATR-IR spectroscopy of pendant NH_2 groups on silica involved in the knoevenagel condensation. *Langmuir* **22**, 3698–3706 (2006).

56. Wiles, D. M. & Suprunchuk, T. The infrared absorption spectra of thiosemicarbazide and related compounds: NH_2 and NH vibrations. *Can. J. Chem.* **47**, 1087–1089 (1969).

57. Milligan, D. E. & Jacox, M. E. Matrix-isolation infrared spectrum of the free radical NH_2. *J. Chem. Phys.* **43**, 4487–4493 (1965).

58. Zheng, W. et al. Self-activated Ni cathode for electrocatalytic nitrate reduction to ammonia: From fundamentals to scale-up for treatment of industrial wastewater. *Environ. Sci. Technol.* **55**, 13231–13243 (2021).

59. Albina, P. et al. Influence of hydrogen electron donor, alkaline pH, and high nitrate concentrations on microbial denitrification: A review. *Int. J. Mol. Sci.* **20**, 5163 (2019).

60. Ahmadi, M. T., Bodaghzadeh, M., Rahimian Koloor, S. S. & Petru, M. Graphene nanoparticle-based, nitrate ion sensor characteristics. *Nanomaterials Basel* **11**, 150 (2021).

61. Liu, H. et al. Electrocatalytic nitrate reduction on oxide-derived silver with tunable selectivity to nitrite and ammonia. *ACS Catal.* **11**, 8431–8442 (2021).

62. Ma, W. et al. Promoting electrocatalytic CO_2 reduction to formate via sulfur-boosting water activation on indium surfaces. *Nat. Commun.* **10**, 892 (2019).

63. Chen, S. et al. Unveiling the proton-feeding effect in sulfur-doped Fe-N-C single-atom catalyst for enhanced CO_2 electroreduction. *Angew. Chem. Int. Ed.* **61**, e202206233 (2022).

64. Su, L. et al. Electrochemical nitrate reduction by using a novel Co_3O_4/Ti cathode. *Water Res.* **120**, 1–11 (2017).

65. Chauhan, R. & Srivastava, V. C. Electrochemical denitrification of highly contaminated actual nitrate wastewater by Ti/RuO_2 anode and iron cathode. *Chem. Eng. J.* **386**, 122065 (2020).

66. Wu, Z. Y. et al. Electrochemical ammonia synthesis via nitrate reduction on Fe single atom catalyst. *Nat. Commun.* **12**, 2870 (2021).

67. Chen, G.-F. et al. Electrochemical reduction of nitrate to ammonia via direct eight-electron transfer using a copper–molecular solid catalyst. *Nat. Energy* **5**, 605–613 (2020).

68. Du, H. et al. Durable electrocatalytic reduction of nitrate to ammonia over defective pseudobrookite Fe_2TiO_5 nanofibers with abundant oxygen vacancies. *Angew. Chem. Int. Ed.* **62**, e202215782 (2023).

69. Liao, P. H., Chen, A. & Lo, K. V. Removal of nitrogen from swine manure wastewaters by ammonia stripping. *Bioresour. Technol.* **54**, 17–20 (1995).

70. Yuan, M.-H., Chen, Y.-H., Tsai, J.-Y. & Chang, C.-Y. Ammonia removal from ammonia-rich wastewater by air stripping using a rotating packed bed. *Process Saf. Environ. Prot.* **102**, 777–785 (2016).

71. Rosca, V., Duca, M., de Groot, M. T. & Koper, M. T. M. Nitrogen cycle electrocatalysis. *Chem. Rev.* **109**, 2209–2244 (2009).

72. Searle, P. L. The berthelot or indophenol reaction and its use in the analytical chemistry of nitrogen. *Analyst* **109**, 549–568 (1984).

73. Carvalho, A. P., Meireles, L. A. & Malcata, F. X. Rapid spectrophotometric determination of nitrates and nitrites in marine aqueous culture media. *Analusis* **26**, 347–351 (1998).

74. Polatides, C. & Kyriacou, G. Electrochemical reduction of nitrate ion on various cathodes – reaction kinetics on bronze cathode. *J. Appl. Electrochem.* **35**, 421–427 (2005).

75. Kresse, G. & Furthmüller, J. Efficiency of ab-initio total energy calculations for metals and semiconductors using a plane-wave basis set. *Comp. Mater. Sci.* **6**, 15–50 (1996).

76. Kresse, G. & Furthmüller, J. Efficient iterative schemes for ab initio total-energy calculations using a plane-wave basis set. *Phys. Rev. B* **54**, 11169–11186 (1996).

77. Perdew, J. P., Burke, K. & Ernzerhof, M. Generalized gradient approximation made simple. *Phys. Rev. Lett.* **77**, 3865–3868 (1996).

78. Kresse, G. & Joubert, D. From ultrasoft pseudopotentials to the projector augmented-wave method. *Phys. Rev. B* **59**, 1758–1775 (1999).

79. Blöchl, P. E. Projector augmented-wave method. *Phys. Rev. B* **50**, 17953–17979 (1994).

80. Methfessel, M. & Paxton, A. T. High-precision sampling for Brillouin-zone integration in metals. *Phys. Rev. B* **40**, 3616–3621 (1989).

81. Nørskov, J. K. et al. Origin of the overpotential for oxygen reduction at a fuel-cell cathode. *J. Phys. Chem. B* **108**, 17886–17892 (2004).

82. Duan, Z. & Xiao, P. Simulation of potential-dependent activation energies in electrocatalysis: Mechanism of O–O bond formation on RuO_2. *J. Phys. Chem. C* **125**, 15243–15250 (2021).

83. Ochterski, J. W. *Thermochemistry in Gaussian* (Gaussian inc, 2000).

84. Gupta, S., Rivera D. J., Shaffer M., Chismar A., Muhich C. Behavior of cupric single atom alloy catalysts for electrochemical nitrate reduction: An ab initio study. *ACS EST Engg.* https://doi.org/10.1021/acsestengg.1023c00207 (2023).

85. Calle-Vallejo, F., Huang, M., Henry, J. B., Koper, M. T. M. & Bandarenka, A. S. Theoretical design and experimental implementation of Ag/Au electrodes for the electrochemical reduction of nitrate. *Phys. Chem. Chem. Phys.* **15**, 3196 (2013).

86. Liu, J.-X., Richards, D., Singh, N. & Goldsmith, B. R. Activity and selectivity trends in electrocatalytic nitrate reduction on transition metals. *ACS Catal.* **9**, 7052–7064 (2019).

87. Qiao, M., Liu, J., Wang, Y., Li, Y. & Chen, Z. $PdSeO_3$ monolayer: Promising inorganic 2D photocatalyst for direct overall water splitting without using sacrificial reagents and cocatalysts. *J. Am. Chem. Soc.* **140**, 12256–12262 (2018).

Author contributions
M.L., W.Liao, J.W., C.L. and J.F. conceived the research and supervised the project. W.Liao and J.W. performed the experiments. M.L., W.Liao, J.W., S.C., Q.W., Y.C., T.L., X.W., Y.W., W.Li, T.C., C.M., H.L., Y.L., W.Liu, J.F. and B.X. analyzed the data. K.L. and G.N. carried out the DFT simulations. W.Liao and C.L. wrote the draft. All authors discussed the results and contributed to the writing of the manuscript.

Competing interests
The authors declare no competing interests.

Additional information
Supplementary information The online version contains supplementary material available at https://doi.org/10.1038/s41467-024-45534-2.

Correspondence and requests for materials should be addressed to Junwei Fu, Beidou Xi or Min Liu.

Peer review information *Nature Communications* thanks Xijun Liu and the other anonymous reviewers for their contribution to the peer review of this work. A peer review file is available.

Reprints and permissions information is available at http://www.nature.com/reprints

Publisher's note Springer Nature remains neutral with regard to jurisdictional claims in published maps and institutional affiliations.